Nano Research

Open Access

Research Article

Superior activity hydrogen evolution enabled by interfacial water orientation and concerted proton–electron transfer

Yuanfeng Gao[1], Junyu Wang[1], Yusheng Yang[1], Liang Wu[2], Aimin Yu[3], Dong-sheng Li[4], Cunman Zhang[1], Chenghua Sun[3], and Hong Lv[1] ✉

[1] *Clean Energy Automotive Engineering Center, School of Automotive Studies, Tongji University, Shanghai 200092, China*
[2] *Shanghai Electric Group, Shanghai Hydrogen Energy Times Technology Co., LTD, Shanghai 200050, China*
[3] *Department of Chemistry and Biotechnology Swinburne University of Technology Swinburne, VIC 3122, Australia*
[4] *College of Materials and Chemical Engineering Key Laboratory of Inorganic Nonmetallic Crystal-line and Energy Conversion Materials China, Three Gorges University, Yichang 443002, China*

Cite this article: *Nano Research*, **2026**, *19*, 94908648. https://doi.org/10.26599/NR.2026.94908648

ABSTRACT: Proton transfer (PT) at the catalyst-electrolyte interface is a fundamental step in the hydrogen evolution reaction (HER), yet its interfacial dynamics is poorly understood. Here, we report 15% Co/O-FeP supported on multiwalled carbon nanotubes (MWCNTs) as a highly efficient HER catalyst, delivering an overpotential of only 58 mV at 10 mA·cm^{-2} and sustaining 500 mA·cm^{-2} for over 111 h without noticeable degradation. Outstanding HER performance and high-current stability make industrial-level hydrogen evolution feasible. Using *in-situ* Raman spectroscopy and *ab initio* molecular dynamics (AIMD) simulations, we reveal that the orientation of interfacial water molecules, particularly interfacial H$^+$ solvation effect induced by H-down configurations, governs HER kinetics by accelerating proton migration and enabling a concerted proton-electron transfer (CPET). Mechanically, PT proceeds through a two-step pathway: (i) Protons migrate from bulk solution to the electrical double layer (EDL) to form H_3O^+ and (ii) H_3O^+ undergoes rapid proton exchange with catalyst active sites. H-down water configurations within the inner Helmholtz plane (IHP) stabilizes de-solvation shells and couples efficiently with interfacial electrons, lowering kinetic barriers. These findings establish a direct correlation between interfacial water structure, hydrogen-bond network, and CPET efficiency, providing fundamental insights for the rational design of advanced electrocatalytic interfaces.

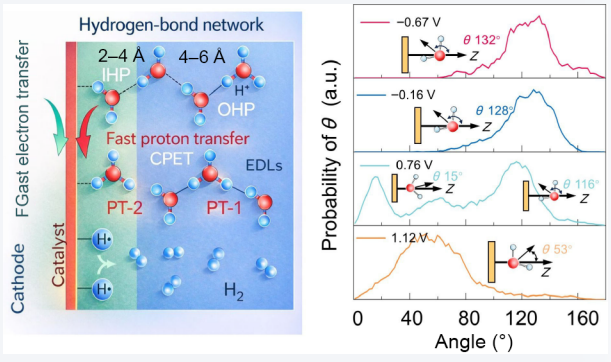

KEYWORDS: hydrogen bond network, concerted proton-electron transfer (CPET), interfacial water structure, interfacial solvation effect, high current density

1 Introduction

Hydrogen, recognized as an environmentally sound and efficient energy carrier, offers versatile integration with diverse energy systems like ammonia and hydrocarbons. However, conventional methods of hydrogen production inevitably result in significant carbon dioxide emissions. Capitalizing on the green electrons produced by renewable energy sources for hydrogen (H_2) generation presents a promising approach to address the imperative of sustainable energy conversion [1–3]. In addition, by storing excess electrical energy in the form of chemical energy, the technology effectively balances the mismatch between intermittent solar/wind energy and the existing grid's need for continuous power.

The hydrogen evolution reaction (HER) operate under acidic conditions, heavily depends on the rare and costly precious metal platinum (Pt) [4]. Relying on Pt significantly increases the costs of hydrogen production, hindering the widespread adoption of industrial-scale hydrogen evolution due to their high expenses. Consequently, the development of efficient transition metal catalysts assumes paramount importance, as it holds the key to diminishing the cathodic side costs of hydrogen production. Low-cost, highly active metal phosphides are emerging as promising alternatives to Pt for HER catalysis [5–8]. Among these phosphides, FeP stands out due to its exceptional stability and rich, tunable

Received: January 17, 2026; **Revised:** February 28, 2026
Accepted: March 17, 2026

✉Address correspondence to lvhong@tongji.edu.cn

electronic structure, showcasing potential to outperform noble metal catalysts in both catalytic performance and economic viability [9–11]. Nonetheless, the HER performance of pure FeP and CoP remains suboptimal, necessitating a range of strategies including coordination engineering, interface engineering, and phase engineering to adjust the hydrogen adsorption free energy (ΔG_{H^*}). The elements in the phosphide leaching under high current, resulting in its stability needs to be further improved.

Proton coupled electron transfer (PCET) plays a crucial role in redox catalytic reactions, bioengineering and energy conversion, especially in acidic HER. The volmer step in the HER reaction involves the PCET reaction, and elucidating whether it occurs sequentially is an important but often challenging task. A PCET reaction through electron transfer followed by proton transfer (ETPT), proton transfer followed by electron transfer (PTET), or in a single, concerted electron–proton transfer step (CEPT) [12–17]. Interfacial PCET reactions to form M–H bonds proceed along an adiabatic free energy surface with a single reaction barrier corresponding to a single CPET step [18, 19]. The mechanism of triggering CPET is conducive to the rapid interaction of protons and electrons to form the key intermediate H* of HER, which reduces the activation energy of the reaction and greatly enhances the production rate and efficiency of H_2. However, the CPET mechanism in HER is hard to be triggered, which is mainly reflected in the asynchronous transfer of electrons and protons, which will inevitably increase the reaction path and activation energy of HER [19, 20]. The slow proton transfer rate at the catalyst interface in HER is the main factor that makes it challenging to trigger the CPET process [18, 21, 22].

The hydrogen evolution and oxidation reactions (HER/HOR) essentially involve a proton transfer (PT) process through the Volmer and Heyrovsky steps. This process typically comprises two PT steps: (i) proton transfer through the hydrogen bond network (HBN) in the bulk solution to the electrical double layer (EDL) region (PT-1) and (ii) hydrogen transfer between water molecules at the electrode surface and within the inner Helmholtz plane (IHP) (PT-2) [23]. Previous studies have been focused on studying how the configuration of interfacial water molecules affects PT [24], and the influence of hydrogen-bond network connectivity has received considerably less attention. Protons migrate through HBN via the Grotthuss mechanism [25–27], and the strength of H-bond plays a crucial role. Typically, the strength of the hydrogen bond is associated with the distance between oxygen atoms in hydrogen-bonded water molecules [25]. Dereka et al. proposed that the hydrogen bond (H-bond) leads to higher proton vibrational frequencies in aqueous KHF_2 [25]. Guo et al. proposed an interlayer confinement strategy to generate short strong H-bonds (SHBs) networks for the development of highly conductive hydroxide exchange membranes (HEMs) [26]. These insights can be integrated into the early stages of catalyst design, allowing researchers to develop effective synthetic strategies to optimize catalytic performance. Metal centers and defect sites induce specific orientations of water molecules (such as H-down or H-up configurations) through electrostatic interactions, while functional groups and ligands modulate hydrogen bond strength through hydrogen bonding. The metal centers, functional groups, ligands, and defect structures of catalysts essentially influence the interfacial water structure, hydrogen bond length, and HBN connectivity during PT by altering the interfacial electric field, local charge distribution, and geometric constraints.

However, the *ab initio* molecular dynamics (AIMD) simulations reveal that the frequency of proton transfer does not always correlate positively with hydrogen bond strength in this study. Detailed analysis of the HBN connectivity shows that, under more negative potentials, although the average H-bond length decreases, the HBN becomes significantly disrupted around ~ 9.5 Å, resulting in a reduced proton transfer frequency. Nevertheless, the HER solid-liquid interface still faces the following challenges: (i) design the charge distribution at the catalyst interface to achieve the inversion of the water configurations at the interface; (ii) how H-bond length and the flexibility/rigidity of HBN govern its connectivity; (iii) precision probing of interfacial water structures demands finer-resolution operando spectroscopy.

In acidic HER, we observed that the asynchronous transfer of protons and electrons at the interface between the catalyst and the EDL influences the rate-determining step (RDS) of the overall reaction. Modulating the chemical coordination environment on the catalyst surface (via controlled Co doping) alters the interfacial water structure, thereby affecting the PT rate and efficiency with a specific proton donors [28]. The presence of unsaturated coordination sites in the amorphous phase promotes the formation of a hydrogen bond network at the catalytic interface, which facilitates rapid proton transfer to the active sites. Modulating the interfacial water structure further strengthens the hydrogen bond network, thereby accelerating proton transfer to the active sites [29]. Concurrently, constructing amorphous core–shell structures on multi-walled carbon nanotubes (MWCNTs) endows the catalyst with superior charge transport capabilities. Benefitting *in-situ* EIS, proton transfer and electron transfer in HER can be distinguished at different frequencies. The time constants derived from these frequencies are used to describe the relative steps of HER, thereby determining the trends of PT and electron transfer (ET) with potential changes. By integrating electrochemical kinetic analyses, this study collectively elucidates the specific mechanisms underlying HER, offering a foundation for the meticulous tuning of the catalyst's coordination structure for optimal performance. The study here unveils that the HBN of bulk water in the PT-2 process needs to maintain a moderate rigidity, and makes it sufficiently flexible for dynamic rearrangement and efficient charge transfer. Furthermore, the study examines the interfacial water structure at the catalytic interface, highlighting its critical role in proton conveyance within the hydrogen bond network, offering valuable insights for future catalyst interface design. By leveraging coordination engineering in amorphous materials to induce a CPET effect, this strategy presents an innovative approach for developing HER catalysts capable of operating efficiently at high current densities.

2 Results and discussion

The 15% Co/O-FeP/MWCNTs, CoP/MWCNTs, FeP/MWCNTs electrocatalysts were synthesized through the same method (detailed procedures are given in the experimental section, and illustrated in Fig. S1 in the Electronic Supplementary Material (ESM). Figure 1(a) shows the X-ray diffraction (XRD) pattern of 15% Co/O-FeP/MWCNTs, the main diffraction peaks in at 32.78° correspond to the (002) crystal planes of CoP, and 48.37° correspond to the (202) crystal planes of FeP, indicating the successful incorporation of Co into the FeP lattice. The actual Co doping level in 15% Co/O-FeP/MWCNTs was determined by ICP-

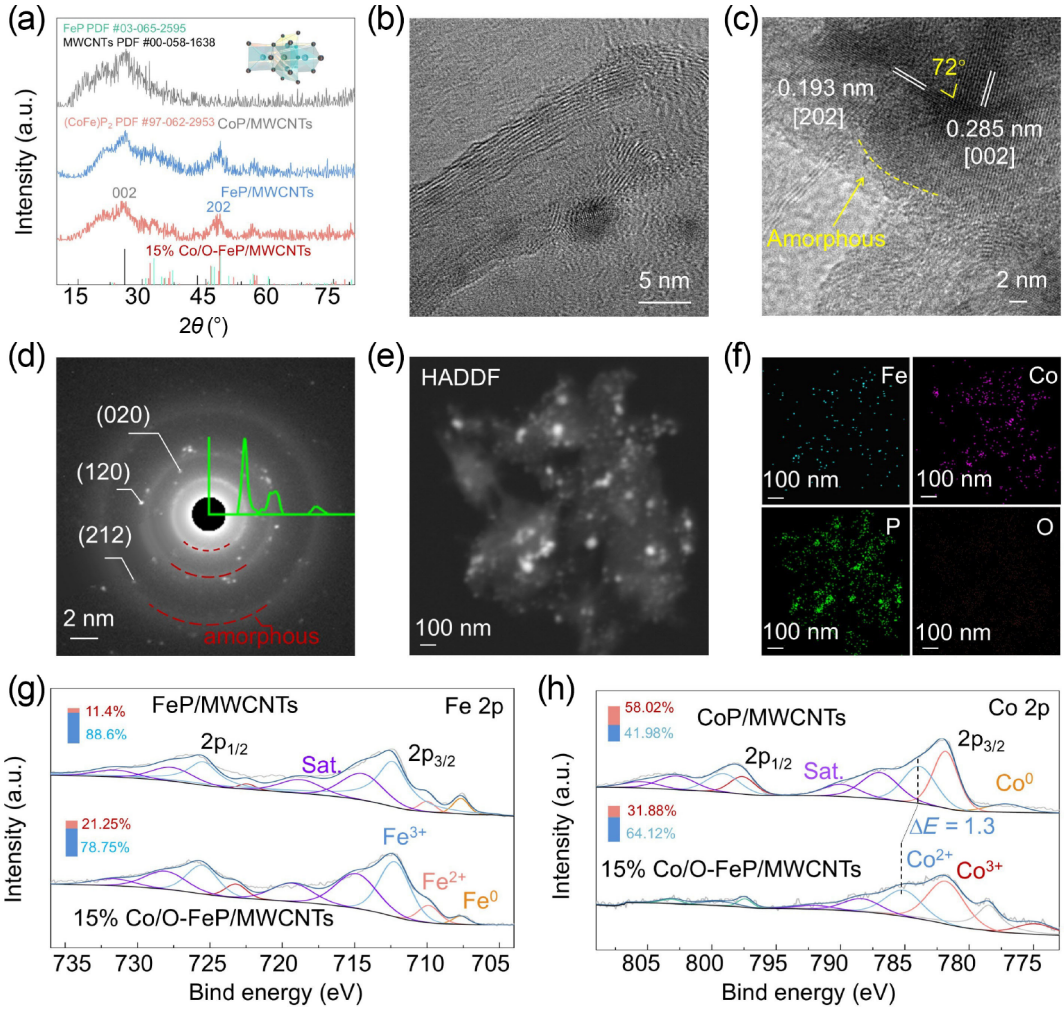

Figure 1 Structural characterizations of 15% Co/O-FeP/MWCNTs. (a) XRD patterns of CoP/MWCNTs, FeP/MWCNTs, and 15% Co/O-FeP/MWCNTs. (b) and (c) HR-TEM images of 15% Co/O-FeP/MWCNTs. (d) SAED pattern of 15% Co/O-FeP/MWCNTs. (e) HAADF-STEM image and (f) the corresponding STEM-EDS mappings of 15% Co/O-FeP/MWCNTs. (g) High-resolution XPS spectra of Fe 2p for FeP/MWCNTs and 15% Co/O-FeP/MWCNTs. (h) High-resolution XPS spectra of Co 2p for CoP/MWCNTs and 15% Co/O-FeP/MWCNTs.

OES to be 14.22%, which is close to the 15% proportion of Co salt used in the synthesis. The TEM images (Figs. 1(b) and 1(c)) show that 15% Co/O-FeP nanoparticles uniformly grow on MWCNTs, with a particle size of approximately 3.58 nm (Fig. S5 in the ESM). Figure 1(d) shows that lattice spacings of 0.193 and 0.285 nm correspond to the [202] and [002] crystal planes, respectively, aligning well with the XRD data for FeP (Fig. S6 in the ESM). The yellow dashed line separates the crystalline and amorphous regions. The selected area electron diffraction (SAED) pattern (Fig. 1(e)) of 15% Co/O-FeP/MWCNTs reveals both crystalline and amorphous characteristics, indicating an amorphous/crystalline core-shell structure. The high-resolution transmission electron microscopy (HRTEM) and high-angle annular dark-field (HAADF) scanning transmission electron microscopy (STEM) observations, along with the corresponding energy-dispersive X-ray spectroscopy (EDS) mapping (Fig. 1(f)), show that Co is successfully incorporated into the FeP lattice in the nanoparticles, consistent with the XRD analysis results.

High-resolution XPS spectra of 15% Co/O-FeP/MWCNTs was conducted to determine the impact of element doping on the coordination structure and valence state distribution of Fe and Co in the amorphous shell. The Fe 2p spectrum (Fig. 1(g)) of 15% Co/O-FeP/MWCNTs shows that the first doublet at 712.4 and 725.6 eV is ascribed to Fe^{3+} and the second doublet at 710.1 and 722.5 eV is ascribed to Fe^{2+}. The single peak at 707.8 eV in both 15% Co/O-FeP/MWCNTs and FeP/MWCNTs is attributed to metallic Fe [30]. Typical FeP has a six-coordinated octahedral structure with Fe in the +3 oxidation state. The presence of low-valence Fe^{2+} and metallic Fe in 15% Co/O-FeP/MWCNTs and FeP/MWCNTs likely results from the unsaturated coordination structure of the amorphous phase. The other doublets correspond to satellite peaks. The proportion of Fe^{2+} in 15% Co/O-FeP/MWCNTs (Fig. S1 in the ESM) is higher than in FeP/MWCNTs, indicating that Co doping affects the coordination structure of FeP, thereby modulating the Fe^{2+} proportion in the amorphous shell of the catalyst. In the Co 2p spectrum (Fig. 1(h)) of 15% Co/O-FeP/MWCNTs, the peak at 782.8 eV corresponds to Co^{3+} [31], and the peak at 786.1 eV corresponds to Co^{2+}. Compared to the Co 2p spectrum of CoP/MWCNTs, the Co^{2+} peak in 15% Co/O-FeP/MWCNTs shifts to higher binding energy by 1.65 eV, indicating decreased electron density around Co^{2+}, suggesting electron transfer from Co to Fe sites.

Figure 2(a) demonstrates that tuning the Co content in Co/O-FeP/MWCNTs regulates the local coordination enviroment,

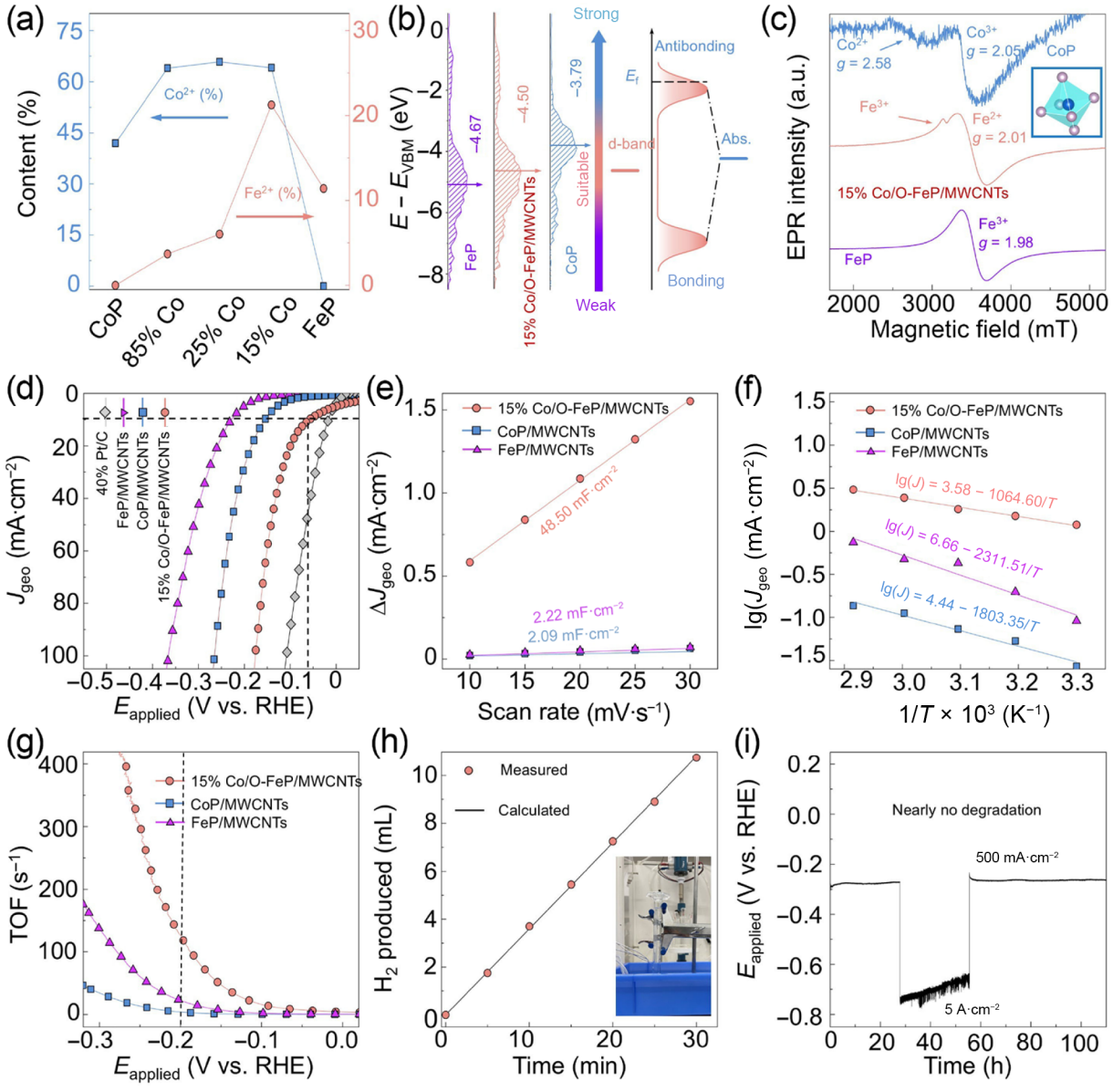

Figure 2 The correlation between electronic structure and HER activity on 15% Co/O-FeP/MWCNTs. (a) Proportion of Co^{2+} and Fe^{2+} in catalysts with different Co levels. (b) High-resolution valence band profiles of Fe relative to the valence band maximum (VBM) for the CoP/MWCNTs, FeP/MWCNTs, and 15% Co/O-FeP/MWCNTs electrodes. (c) EPR spectra of the CoP/MWCNTs, FeP/MWCNTs, and 15% Co/O-FeP/MWCNTs electrodes. (d) HER-LSV curves of 15% Co/O-FeP/MWCNTs, CoP/MWCNTs, FeP/MWCNTs, and 40% Pt. (e) C_{dl} of 15% Co/O-FeP/MWCNTs, CoP/MWCNTs, and FeP/MWCNTs. (f) Arrhenius plots of 15% Co/O-FeP/MWCNTs, CoP/MWCNTs, and FeP/MWCNTs at 10 mA·cm^{-2} overpotential for the HER reaction. (g) TOF plots of 15% Co/O-FeP/MWCNTs, CoP/MWCNTs, and FeP/MWCNTs electrode. (h) Faraday efficiency of HER for 15% Co/O-FeP/MWCNTs with constant current density of 100 mA·cm^{-2}. (i) Chronopnlentinmetry curve of 15% Co/O-FeP/MWCNTs for 111 h

thereby modulating the Fe^{2+} proportion within the catalyst. This trend is consistent with results obtained from XPS analysis. The single peak at 707.8 eV in both 15% Co/O-FeP/MWCNTs and FeP/MWCNTs corresponds to metallic Fe. The O 2p peaks (Fig. S7 in the ESM) at 531.8 and 533.3 eV are attributed to surface oxygen species (O_{surf}) and adventitious species (O_{adv}) respectively [29, 31, 32]. For the data summary of the Fe 2p and Co 2p spectra (Figs. S8–S12 in the ESM), variations in the proportions of Co^{2+} and Fe^{2+} within the catalyst are caused by the differences in Co doping levels [33, 34].

Utilizing the flexibility of the coordination structure of the amorphous shell, Co doping adjusts the coordination around FeP, thereby modulating the electronic structure of Co/O-FeP/MWCNTs [35, 36]. The d-band center of catalytic sites in 15% Co/O-FeP/MWCNTs should shift downward relative to the Fermi level (E_f) compared to CoP/MWCNTs. The d-band centers measured by valence band spectra (Fig. 2(b)) for 15% Co/O-FeP/MWCNTs, CoP/MWCNTs, and FeP/MWCNTs are −4.61, −4.61, and −3.95 eV, respectively, confirming that the d-band center of 15% Co/O-FeP/MWCNTs is positioned between those of CoP/MWCNTs and FeP/MWCNTs after Co coordination [37, 38]. This enhances proton adsorption and desorption at the catalytic sites and facilitates proton transfer from the EDL to the active sites of the catalyst on the electrode [39]. In the electron paramagnetic resonance (EPR) spectra (Fig. 2(c)), the *g*-factors of 2.58 and 2.05 for CoP/MWCNTs correspond to Co^{2+} and Co^{3+}, respectively. The *g*-

factor of 1.98 for FeP/MWCNTs corresponds to Fe^{2+}. The splitting phenomenon of Fe^{3+} was not observed in FeP/MWCNTs, likely because Fe^{3+} in FeP/MWCNTs is in a low-spin state (S = 1/2). The g-factor of 2.01 for 15% Co/O-FeP/MWCNTs corresponds to Fe^{2+}, and the spectrum shows splitting due to Co doping, which alters the coordination structure of FeP, leading to Fe^{3+} in a high-spin state (S = 5/2) [40, 41]. The above characterizations fully demonstrate that the Co-coordinated FeP in the amorphous shell has an excellent electronic structure, with moderate proton adsorption strength, which accelerates the coupling process of protons in the EDL layer and electrons in the electrode.

As shown in Fig. 2(d), the linear sweep voltammetry (LSV) curves of 15% Co/O-FeP/MWCNTs, CoP/MWCNTs, FeP/MWCNTs, and commercial 40% Pt/C indicate that the overpotential of 15% Co/O-FeP/MWCNTs at 10 mA·cm^{-2} is only 58 mV, surpassing the performance of other Co-doped catalysts (Figs. S13 and S14 in the ESM). As the applied potential increases, the current of 15% Co/O-FeP/MWCNTs surpasses that of commercial 40% Pt/C at an overpotential of 232 mV, demonstrating superior high-current performance. To investigate the effect of Co doping on the number of active sites, the double-layer capacitance (C_{dl}) of 15% Co/O-FeP/MWCNTs, CoP/MWCNTs, FeP/MWCNTs, commercial 40% Pt/C, and other Co/Fe ratio Co/O-FeP/MWCNTs was estimated from the CV curves at different scan rates (Figs. S15 and S16 in the ESM). The C_{dl} of 15% Co/O-FeP/MWCNTs (Fig. 2(e)) is 48.5 mF·cm^{-2}, higher than that of CoP/MWCNTs (23.94 mF·cm^{-2}), FeP/MWCNTs (23.94 mF·cm^{-2}), and the other Co/Fe ratio Co/O-FeP/MWCNTs (Fig. S17 in the ESM). Compared to other Co/Fe ratio Co/O-FeP/MWCNTs (Table S2 in the ESM), 15% Co/O-FeP/MWCNTs has the largest electrochemically active surface area (ECSA), indicating that Co coordination affects the number of active sites in Co/O-FeP/MWCNTs. The apparent activation energy of the samples was calculated using the Arrhenius equation (Fig. 2(f) and Figs. S18–S20 in the ESM) to compare the intrinsic catalytic activity of the catalysts. The activation energies of 15% Co/O-FeP/MWCNTs, CoP/MWCNTs and FeP/MWCNTs with overpotential (η_{10}) at 10 mA·cm^{-2} were 20.83, 34.53 and 44.26 kJ·mol^{-1}, respectively, which indicated that 15% Co/O-FeP/MWCNTs had an excellent intrinsic catalytic activity.

To further explore the effect of Co coordination on intrinsic activity, turnover frequency (TOF) was used to determine the specific activity of the catalysts. The TOF of 5% Co/O-FeP/MWCNTs (Fig. 2(g) and Fig. S21 in the ESM) at −0.2 V is 127 s^{-1}, significantly higher than that of FeP/MWCNTs (22 s^{-1}) and CoP/MWCNTs (4 s^{-1}). Co coordination greatly enhances the intrinsic activity of the catalyst, consistent with the apparent activation energy results. Based on the above results, we believe that the enhanced catalytic activity is due to Co coordination regulating the electronic structure of the amorphous surface. The Faradaic efficiency of 15% Co/O-FeP/MWCNTs is nearly 100% (Fig. 2(h)), indicating no electrochemical corrosion. Furthermore, apart from the HER, no side reactions, such as CO_2 reduction, are observed. The chronopotentiometry method was used to test the electrochemical stability of 15% Co/O-FeP/MWCNTs for 111 h (Fig. 2(i)), and the voltage showed almost no decay under a constant current of 500 mA·cm^{-2}, confirming its excellent electrochemical stability at high current densities. Other stability tests (Figs. S22 and S23 in the ESM) also showed that 15% Co/O-FeP/MWCNTs have superior stability compared to 40% Pt/C. We hypothesize that the exceptional stability of 15% Co/O-FeP/MWCNTs, aside from the influence of structural stability, is primarily due to the unique interfacial proton transfer.

Potentiostatic Tafel data were collected from η = 0.018 to 0.388 V, increasing in intervals of 0.02 V in 0.5 M H_2SO_4, as shown in Fig. 3(a). The Tafel slope (Fig. 3(b)) of 15% Co/O-FeP/MWCNTs is 62.3 mV·dec^{-1}, significantly lower than FeP/MWCNTs (81 mV·dec^{-1}) and CoP/MWCNTs (139.2 mV·dec^{-1}). The Tafel slope is crucial for analyzing the HER mechanism but is insufficient alone to determine HER kinetics; it must be combined with other parameters for accurate analysis. When the RDS of HER is the Tafel step, the Tafel slope can be inferred from the coverage of protons on active sites (θ_{H^*}) and the coverage of vacant sites θ^* (where $\theta_{H^*} + \theta^* = 1$) [3]. When the applied voltage (E_{pplied}) and θ_{H^*} are low, the Tafel slope reaches a minimum of 30 mV·dec^{-1}. As θ_{H^*} increases to 0.5, the Tafel slope can reach 60 mV·dec^{-1}. This occurs because θ^* is a function of the applied voltage, and the Tafel slope is a function of θ^* (see Supporting Information for details). Most reports indicate that 40% Pt/C follows the Tafel mechanism in 0.5 M H_2SO_4, with the Tafel slope gradually increasing with voltage. As shown in Fig. 3(b), the Tafel slope of 15% Co/O-FeP/MWCNTs (47.23 mV·dec^{-1}) is similar to 40% Pt/C, suggesting 15% Co/O-FeP/MWCNTs likely follows the Tafel mechanism.

The catalyst's amorphous surface charge (Q) was obtained through pulse voltammetry and quantified by integrating the anodic voltage pulse current response (Figs. S24(b)–S30(b) in the ESM). This method yielded relationship curves among HER current density (J_{geo}), Q, and overpotential ($\eta_{applied}$) (Fig. 3(c) and Figs. S25(c)–S30(c) in the ESM). The Q–$E_{applied}$ and J_{geo}–$E_{applied}$ data points for other catalysts were derived from Tables S3–S11 in the ESM. These curves reveal an interesting phenomenon: A certain amount of Q must accumulate before the HER reaction occurs. Additionally, the faster Q responds to voltage, the smaller the overpotential. The overpotential of 15% Co/O-FeP/MWCNTs is lower than 40% Pt/C at high current density, likely due to fast proton accumulation and transfer kinetics on its surface. As the only charged intermediate in acidic HER is H^+, Q can reflect the real-time accumulation of hydrated hydrogen ions (H_3O^+) in the catalyst surface's Helmholtz outer layer (OHP) and their transfer to the Helmholtz inner layer (IHP) (the process of H_3O^+ shedding its solvation shell). By combining Q with changes in the Tafel slope with $\eta_{applied}$, the kinetic characteristics of HER at different potentials can be analyzed. To further reveal the HER kinetic mechanism, the variation of the reaction order β of lg(J_{geo}) to lg(Q) was studied. As shown in Fig. 3(c), the change in the Tafel slope is symmetrical to the change in β, and their relationship reveals a deeper HER kinetic mechanism. Extensive experiments confirm that β and the Tafel slope share a common feature: the inflection point corresponds to a consistent overpotential (Figs. S25(c)–S30(c) in the ESM). Before the inflection point, 15% Co/O-FeP/MWCNTs has a larger β_1 (18.2) (Fig. 3(c)), likely due to the CPET effect triggered by proton-coupled electron transfer in the Volmer step, which requires substantial proton accumulation. After the inflection point at higher potentials, β_2 (4.4) decreases, indicating reduced dependence of subsequent reactions on proton accumulation. The rate law predicts a decrease in the reaction order of J_{geo} to the proton donor Q, leading to an increase in the Tafel slope, consistent with experimental results (Fig. 3(c)). At this stage, hydrogen adsorption (H_{ad}) on 15% Co/O-FeP/MWCNTs approaches saturation, and the Tafel step rate depends on the combination of two H_{ad} on the

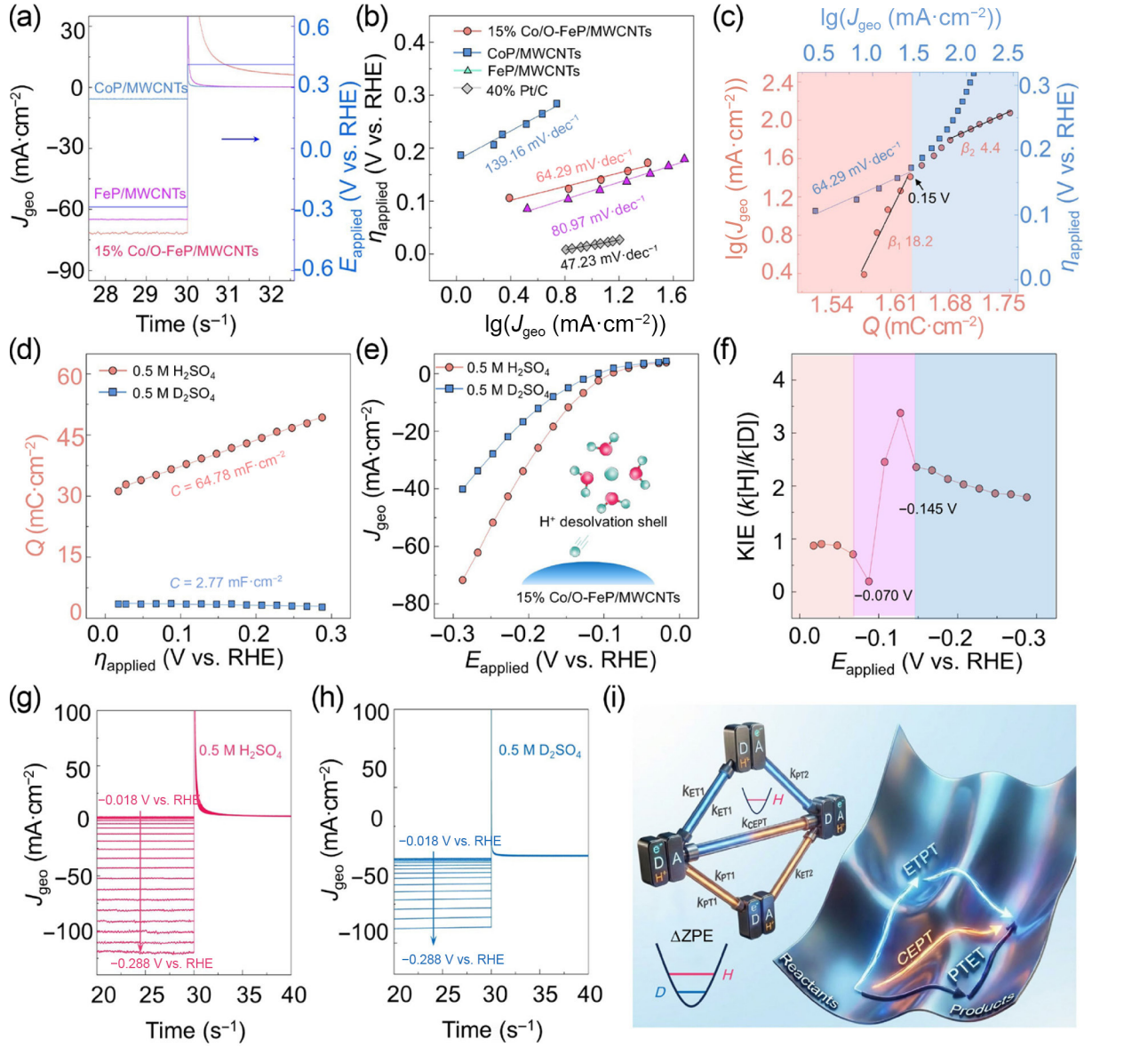

Figure 3 Kinetic and mechanistic analysis of 15% Co/O-FeP/MWCNTs. (a) Representative pulse voltammetry protocol showing the reductive (−0.2875 V vs. RHE) potential-OCP step and the corresponding pulse current response. (b) Tafel plots of 15% Co/O-FeP/MWCNTs, CoP/MWCNTs, FeP/MWCNTs, and 40% Pt were derived from pulse voltammetry. (c) The relationship of lg (J_{geo}) vs. lg(Q) and $\eta_{applied}$ vs. lg (J_{geo}) in the whole potential region of −0.0175 to −0.3875 V vs. RHE. (d) The relationship of Q vs. $\eta_{applied}$ was investigated in 0.5 M H_2SO_4 and 0.5 M D_2SO_4 electrolytes for 15% Co/O-FeP/MWCNTs. (e) HER-LSV curves of 15% Co/O-FeP/MWCNTs were derived from pulse voltammetry (Fig. S18 in the ESM). (f) The ratio of the current density in 0.5 M H_2SO_4 and 0.5 M D_2SO_4 electrolytes for 15% Co/O-FeP/MWCNTs. Section of the pulse voltammetry protocol showing an oxidative and reductive pulse with the current response for 15% Co/O-FeP/MWCNTs in (g) 0.5 M H_2SO_4 and (h) 0.5 M D_2SO_4. (i) Illustration of the three main mechanisms for PCET of HER in acid, each with a distinct transition state, the above-mentioned KIE effect derived from different mechanism and transition states.

surface, not on electrode potential. The stepwise PT-ET pathway is limited by the sluggish PT and the rate difference between PT and ET. According to the law of mass action, if the PT-ET mechanism is followed after the turning potential, β_2 would not decrease, contradicting the experimental results. The change from β_1 to β_2 in 15% Co/O-FeP/MWCNTs confirms that the Volmer step triggers the CPET effect.

The rapid accumulation and conduction of protons in the electric double layer on 15% Co/O-FeP/MWCNTs surface trigger the CPET effect, achieving efficient HER. The CPET process is characterized by kinetic isotope effect (KIE), expressed as the ratio of reaction rates using hydrogen or deuterium sources (KIE = k[H]/k[D]) [42]. Proton accumulation in the OHP and rapid transfer to the IHP involve key intermediate steps of chemical bond breaking and formation. This elucidates the kinetic mechanism of proton transfer in the IHP. Since protons directly participate in the transfer process, substituting them with deuterium (H to D) significantly affects the reaction rate. The mass difference between H and D influences vibrational frequencies and zero-point energy (ZPE), resulting in large KIE. For instance, the KIE of carbon paper are smaller (Fig. S31 in the ESM), usually ranging from 0 to 1, are derived from isotopic substitution occurs at sites not directly involved in proton transfer. Solvent polarity, hydrogen bonding networks, and other factors significantly influence the proton

transfer path and transition state stability in CPET reactions, affecting KIE. The accumulated charges Q (Fig. 3(d)) in the OHP of 15% Co/O-FeP/MWCNTs are 64.8 and 2.8 mF·cm^{-2} in 0.5 M H_2SO_4 and 0.5 M D_2SO_4 aqueous solutions, respectively. The high number of active sites and optimized d-band center position of 15% Co/O-FeP/MWCNTs enhance the catalyst's adsorption capacity for H_3O^+, leading to the significant difference in accumulated charges Q. As shown in Fig. 3(e), steady-state current J_{geo} vs. $E_{applied}$ data (Fig. S32 in the ESM) obtained by pulse voltammetry showed the trend of KIE with $E_{applied}$. In the range of 0 to −0.070 V (RHE), 15% Co/O-FeP/MWCNTs shows no significant KIE (Fig. 3(f)), PT has not occurred at the moment. In the range of −0.070 to −0.145 V (RHE), 15% Co/O-FeP/MWCNTs exhibits a significant KIE effect (KIE > 2), coinciding with the β_1 voltage range, indicating that proton accumulation and rapid transfer trigger the CPET effect at this stage [43]. It is noteworthy that from −0.145 to −0.3 V (vs. RHE), the KIE effect decreases, which may be attributed to hindered proton transfer. Another possible explanation is that the RDS of HER is no longer the CPET process, but instead be governed by the recombination of two H_{ad}, consistent with the previous analysis of $\beta_1 \rightarrow \beta_2$. The formation of a hydrogen-bonding network is crucial for proton accumulation and rapid transfer. The hydrogen-bonding network with a specific structure facilitates triggering the CPET effect. The step current testing reveals that the reaction current in 0.5 M H_2SO_4 solution (Fig. 3(g)) significantly exceeds that in 0.5 M D_2SO_4 (Fig. 3(h)) at identical voltages. This substantial performance disparity arises from deuterium-induced sluggish proton transfer, which shifts the adsorbed H* pathway to a proton-coupled electron transfer (PTET) mechanism. Consequently, the reaction inevitably traverses a higher potential energy surface (Fig. 3(i)).

Previous studies have shown that the connectivity of hydrogen-bond networks within the EDL varies significantly, leading to substantial kinetic pH effects [23]. The connectivity of hydrogen-bond networks is crucial for proton transfer in the EDL, and the structure-function relationship of these networks is closely linked to interfacial water structure [44–46]. *In-situ* Raman spectroscopy was performed to reveal the structure of interfacial water (Fig. 4(a)). The Gaussian peaks in the 2100–3900 cm^{-1} range can be deconvoluted into four peaks at 2971, 3222, 3435, and 3626 cm^{-1}, corresponding to $(HOH)_nH^+$ (hydrogen-bonded water, HBW_n), four-hydrogen-bonded water (4-HBW), two-hydrogen-bonded water (2-HBW), and dangling O–H water. HBW_n and dangling O–H water possess an H-down structure. Spectroscopic and calculated results (Figs. 4(b) and 4(c)) clearly reveal potential-dependent transformations in the structure, composition, and hydrogen bond networks of surface-confined interfacial water on $Co_{0.15}Fe_{0.85}P$/MWCNTs. The vibrational frequencies of the OH bands vary with electrode potential, attributed to the vibrational Stark effect [47]. As shown in Fig. 4(b), the slope for $(HOH)_nH^+$ is 73.16 cm^{-1}·V^{-1}, and for dangling O–H water, it is 41.95 cm^{-1}·V^{-1}, both much larger than those for 4-HBW and 2-HBW. This indicates a large amount of H-down structure inthe EDL of $Co_{0.15}Fe_{0.85}P$/MWCNTs, significantly altering the hydrogen-bond network connectivity of interfacial water molecules. Weak or broken hydrogen bonds result in increased vibrational frequencies (blue shift), indicating an accelerated process of H_3O^+ desolvation and faster proton transfer from OHP to IHP within the EDL [48]. The steeper Stark slope of the $(HOH)_nH^+$ species indicates a closer distance between the electrode and the H atom of water than the 2-HBW and 4-HBW species.

To investigate which type of interfacial water structure facilitates proton transfer, we conducted a quantitative analysis (Table S12 in the ESM) of four water structures as a function of voltage. As shown in Fig. 4(c), with increasing bias voltage, 4-HBW content gradually decreases, 2-HBW remains almost constant, and the H-down structure gradually increases, indicating the H-down structure is the primary factor influencing proton transfer efficiency. To explore changes in interfacial water structure after voltage removal, we quantitatively analyzed the H-down structure at −0.4 V and after bias removal. Experimental results (Fig. 4(e)) confirm that the H-down structure accelerates proton transfer efficiency within the hydrogen-bond network and that the H-down structure may be converted from 2-HBW. XPS O 1s spectra under voltage (Fig. 4(d)) show a highly ordered interfacial water layer on the catalyst surface, confirming that enhancement of the hydrogen-bond network promotes proton transfer efficiency. To verify the interfacial water structure observed via Raman spectroscopy, AIMD simulations were employed to investigate the molecular structure of water at the solid–liquid interface of 15% Co/O-FeP/MWCNTs (Fig. 4(f)). At a potential of −0.16 V (Fig. 4(g)), water molecules at the interface exhibited oriented alignment, predominantly adopting an H-down configuration (Fig. 4(f)). This result is consistent with the observations from *in-situ* Raman spectroscopy.

To elucidate how proton transfer triggers the CPET effect, *in-situ* EIS (Figs. S33(a)–S35(a) in the ESM) was conducted to monitor proton and electron transfer. The essence of EIS is its real-time response to different HER steps at specific voltages, allowing real-time monitoring of the sequence of HER reaction steps and thus determining the specific mechanism of the HER. As shown in Fig. 5(a), EIS data are typically analyzed using an equivalent circuit model to simulate ET and PT processes in HER. The second parallel components (CPE2 and R_2) reflect the hydrogenadsorption behavior on catalyst surface, where C_φ and R_2 represent the hydrogen adsorption pseudo-capacitance and resistance, respectively [49]. As shown in Fig. S36 in the ESM, the integration of C_φ vs. η profiles provides information on the hydrogen adsorption charge (Q_H) on the catalyst surface during HER. The detailed EIS fitting data of 15% Co/O-FeP/MWCNTs, CoP/MWCNTs and FeP/MWCNTs are shown in Tables S13–S15 in the ESM. Within the potential range of 0.007 to 0.148 V, substantial PT occurs in the EDL of 15% Co/O-FeP/MWCNTs, triggering the CPET effect. Both KIE and β show transitions in the similar voltage range (−1.45 to −1.5 V), indicating that the RDS shifts from the CPET-dominated Volmer step to the Tafel step.

The relationship between applied overpotential ($\eta_{applied}$) and adsorption resistance ($\lg R_2$) forms a Tafel-like relationship (Fig. 5(b)), used to explore electron transfer kinetics in HER. The slope for 15% Co/O-FeP/MWCNTs is 100 mΩ·dec^{-1}, smaller than CoP/MWCNTs (205 mΩ·dec^{-1}) and FeP/MWCNTs (122 mΩ·dec^{-1}), indicating high interfacial charge transfer efficiency. As shown in Fig. 5(c), the hydrogen adsorption free energy (ΔG_H) of 15% Co/O-FeP/MWCNTs is −0.16 eV, closer to 0 eV than that of Pt (111, ΔG_H = −0.29 eV). This indicates optimal ΔG_H consistent with the d-band center analysis. The excessively strong ΔG_H of CoP/MWCNTs (−0.56 eV) causes electron accumulation at the solid-liquid interface, impeding electron transfer and resulting in increased charge transfer resistance (205 mΩ·dec^{-1}). Conversely, the weaker ΔG_H of FeP/MWCNTs (0.23 eV) leads to decoupling between H^+ and electron transfer, where PT constrains electron transfer kinetics, slowing interfacial electron transfer

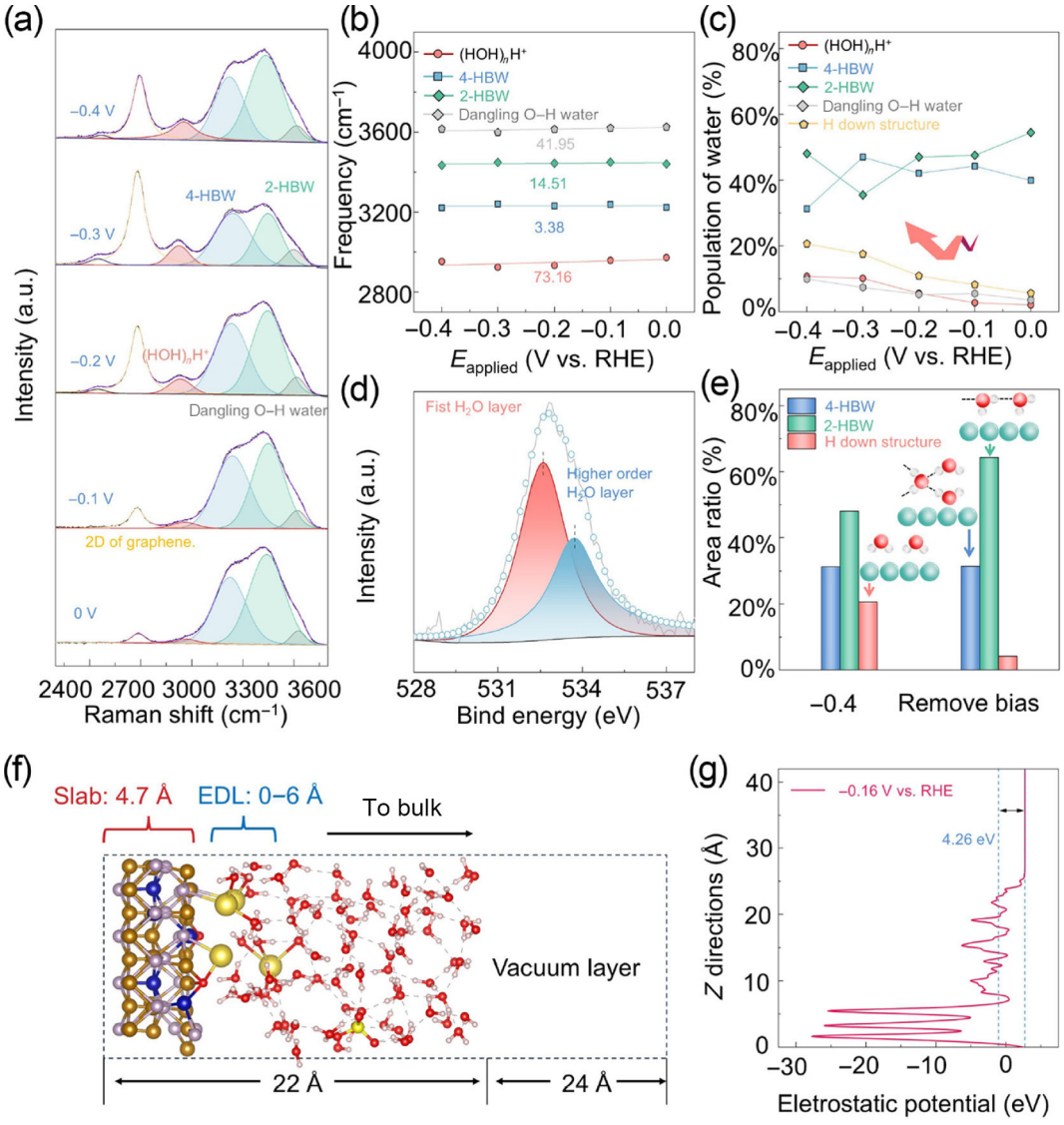

Figure 4 Interfacial water orientation distribution on the catalyst surface. (a) The *in-situ* Raman spectra of 15% Co/O-FeP/MWCNTs and corresponding specific peak intensity of various peak conducted form Raman spectra. (b) Raman peak shifts for various ligand water structures. (c) Percentage content of different coordination water structures on 15% Co/O-FeP/MWCNTs surface. (d) O 1s spectra for 15% Co/O-FeP/MWCNTs after electrochemical treatment. (e) Area ratios for three types of interfacial water structures on 15% Co/O-FeP/MWCNTs at −0.4 V (15 min) and removed bias (30 min). (f) The theoretical model of 15% Co/O-FeP/MWCNTs (202)/water interface at potential of −0.16 V (RHE) condition. (g) Work function estimation for 4 Na by DFT calculations.

(122 mΩ·dec^{-1}). As bias voltage increases, the EIS-Bode plot (Fig. S33(b) in the ESM) for 15% Co/O-FeP/MWCNTs shows a smaller phase angle at low frequencies compared to CoP/MWCNTs and FeP/MWCNTs (Figs. S34(b) and S35(b) in the ESM), indicating higher interfacial charge transfer efficiency. The larger phase angle for CoP/MWCNTs suggests that the capacitive effect dominates, leading to low interfacial charge transfer efficiency.

The response speed of ET and PT to voltage in EIS can be expressed by time constants, providing a powerful tool for analyzing the PCET mechanism [50]. The interfacial ET time constant (Fig. 5(d) and Table S16 in the ESM) for 15% Co/O-FeP/MWCNTs is 10^{-4} s. As shown in Fig. 5(e), the decrease in negative bias voltage enables PT-1 (OHP) and PT-2 (IHP) transfer at the solid–liquid interface to proceed unimpeded by hydrogen adsorption free energy (ΔG_H), thereby completing H^+ desolvation shell and interfacial transfer, coupling with electrons to trigger the CPET. The interfacial ET time constant for CoP is 10^{-2} s (Fig. S37(a) and Table S18 in the ESM), indicating significant impediments to interfacial ET, consistent with its Bode plot. The excessively strong proton adsorption by CoP/MWCNTs prevents desorption, resulting in sluggish interfacial charge transfer kinetics, which aligns with the τ_1 value (10^{-2} s). The intersection of PT and ET time constants confirms that the slow kinetics of PT is influenced by ET. In CoP, slow interfacial charge transfer leads to the accumulation of negative charge, causing interfacial water configuration to invert and disrupting PT-1 process (Fig. 5(f)) within the hydrogen-bond network, the RDS is volmer mechanism. The interfacial ET time constant for FeP is 10^{-4} to 10^{-5} s (Fig. S37(b) and Table S17 in the ESM), and rapid ET transfer is consistent with the Bode plot analysis. For FeP, its ET time constant is significantly affected by $E_{applied}$, leading to the decoupling of PT and ET (Fig. 5(g)). An excessively weak ΔG_H prevents H^+ desolvation solvation shell, which results in an excessively slow PT-2 process, with the Heyrovsky mechanism being the RDS.

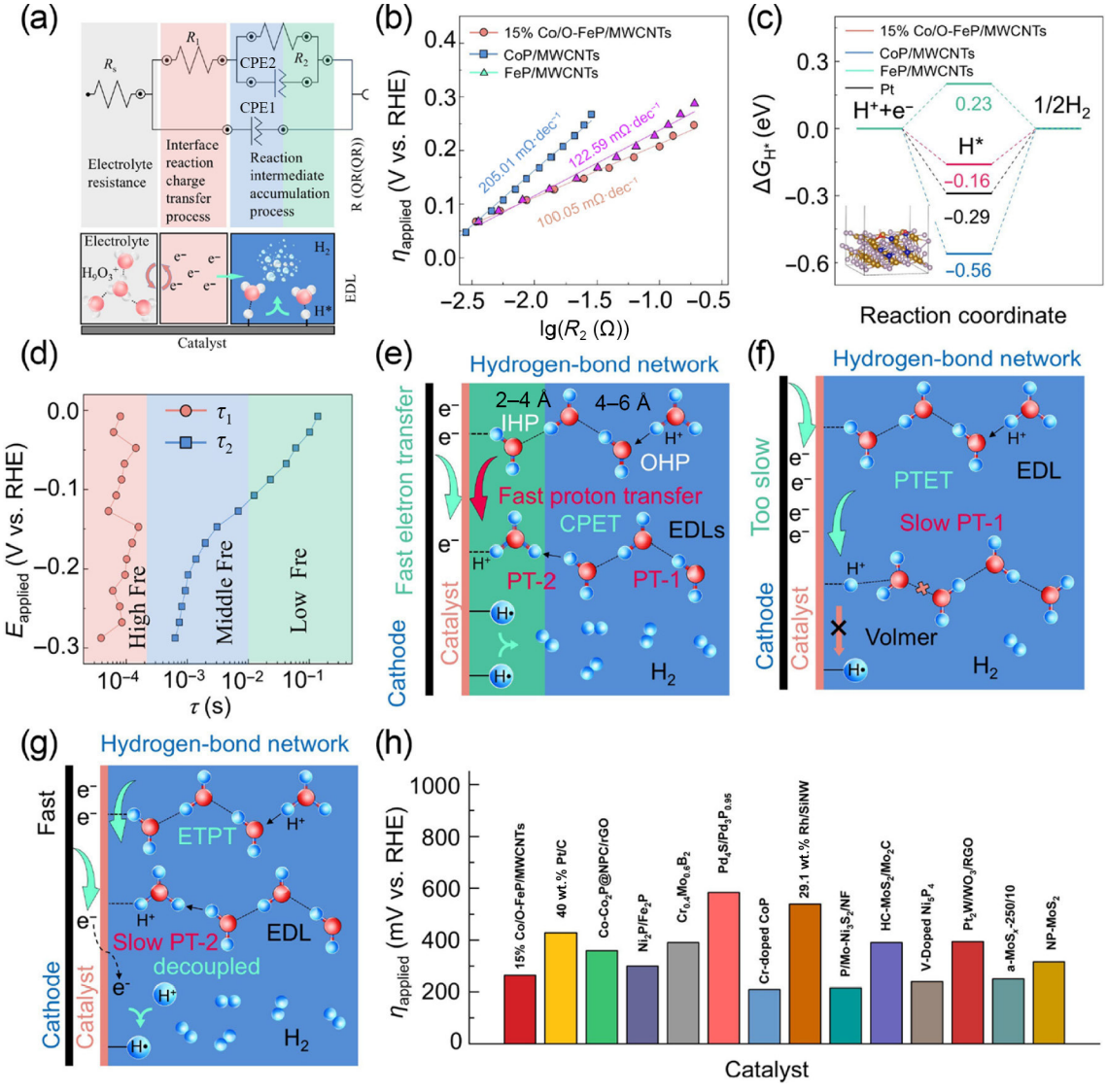

Figure 5 Derivation of the HER specific mechanism and extrapolation of the rate-determining step. (a) Schematic diagram of HER mechanism and corresponding equivalent circuit for 15% Co/O-FeP/MWCNTs. (b) EIS-derived simulated Tafel plots of the 15% Co/O-FeP/MWCNTs, CoP/MWCNTs, and FeP/MWCNTs catalysts. (c) Calculated free energy profiles of HER at the equilibrium potential for 15% Co/O-FeP/MWCNTs, CoP/MWCNTs, FeP/MWCNTs and metal Pt (111). (d) Correlation of the equivalent resistances (R_1 and R_2), time constants ($\tau_1 < \tau_2$) and potentials for 15% Co/O-FeP/MWCNTs (in 0.5 M H_2SO_4) during HER. (e) Schematic illustration of the rapid transfer of protons through the hydrogen bonding network in the EDL of 15% Co/O-FeP/MWCNTs triggering the CPET effect in 0.5 M H_2SO_4. (f) The slow PT-1 in the hydrogen bonding network in the EDL of CoP/MWCNTs triggering the PTET effect in 0.5 M H_2SO_4. (g) The slow PT-2 in IHP of FeP/MWCNTs triggering the PTET effect in 0.5 M H_2SO_4. (h) Overpotentials of 15% Co/O-FeP/MWCNTs at 500 mA·cm^{-2}, with other recently reported HER electrocatalysts in 0.5 M H_2SO_4.

This indicates that in designing and optimizing the electrocatalytic HER process, it is essential to balance proton adsorption strength with interactions among other reaction and transfer steps to trigger the CPET effect in the Volmer step. As shown in Fig. 5(h), the overpotential for 15% Co/O-FeP/MWCNTs at 500 mA·cm^{-2} is only 268 mV, demonstrating significant hydrogen production potential due to its excellent HER kinetics.

To investigate the intrinsic mechanism by which interfacial water configurations and HBN connectivity regulate CPET, AIMD simulations were performed on 15% Co/O-FeP/MWCNTs. Simultaneously, DFT calculations reveal that the hydrogen adsorption free energy (ΔG_H = 0.16 eV) of 15% Co/O-FeP/MWCNTs (Fig. 5(c)) is more desirable than that of Pt (111). This indicates enhanced proton adsorption and desorption kinetics, which is consistent with the d-band center analysis (Fig. 2(d)). The potential of zero charge (PZC) and other potentials at the solid–liquid interface are determined from work function calculations (Figs. S41(b)–S49(b) in the ESM) [51]. Figure 6(a) shows the distributions of oxygen density (ρ_O) and hydrogen density (ρ_H) along the surface normal direction at −0.16 V (RHE). The corresponding values of ρ_O and ρ_H are 0.048 and 0.910 mol·cm^{-3}, respectively, which are consistent with the typical density profile of water. In the IHP (0–4 Å), the hydrogen density peaks at 2.99 Å, while the oxygen density peaks at 3.88 Å, indicating that hydrogen atoms tend to be closer to the electrode surface. The density profile at other potentials are shown in Fig. S38 in the ESM, where hydrogen in water tends to move away from the electrode surface at 1.12 V (RHE).

To further understand water configurations within the IHP, we analyzed the angle θ between the water bisector and the surface

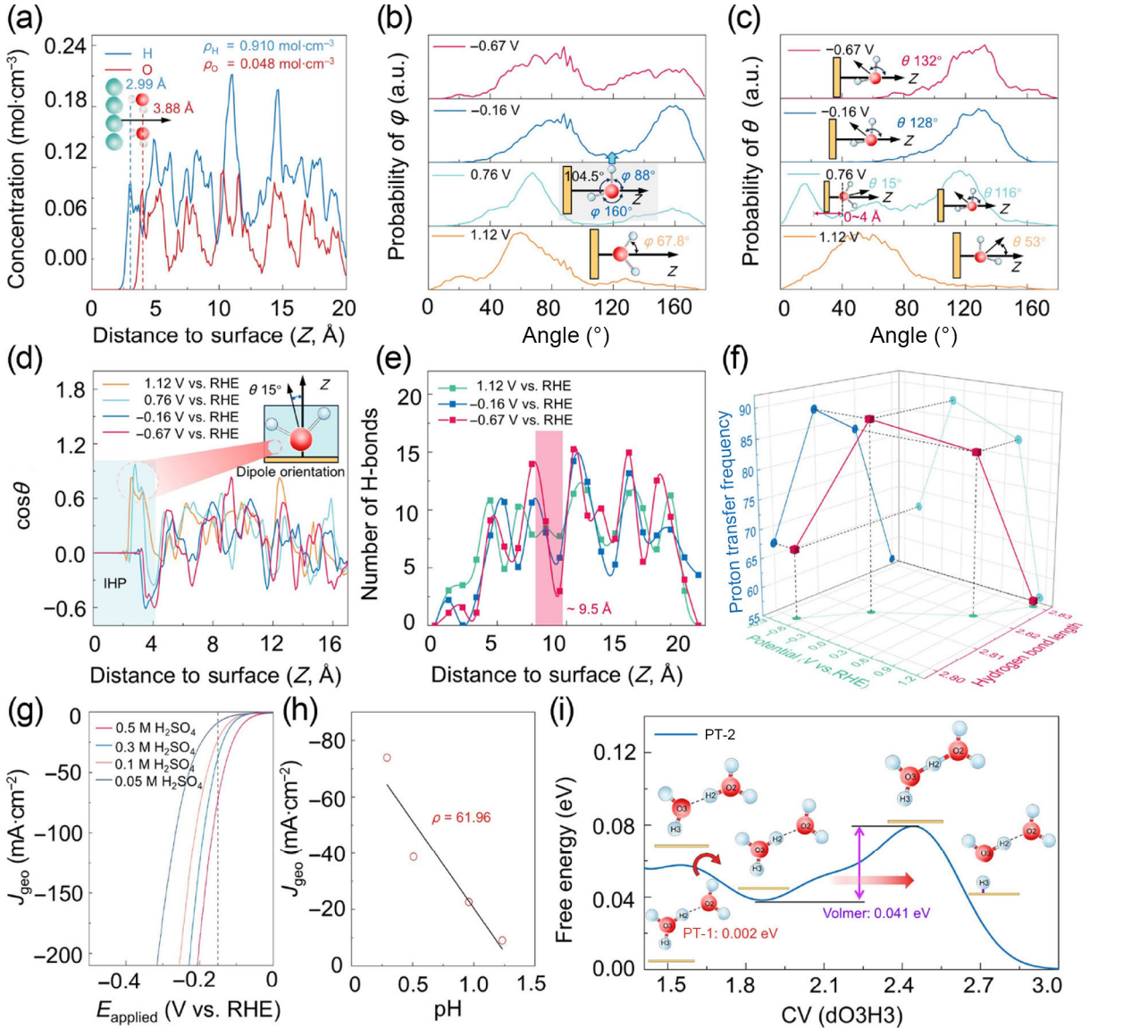

Figure 6 Potential dependence of the interfacial water structure at the electrified 15% Co/O-FeP/MWCNTs (202) surface from AIMD simulations. (a) Concentration distribution profiles of O and H atoms in water along the surface normal direction at −0.16 V vs. RHE. The vertical dashed lines represent the distance of the H and O atoms in the IHP from the surface. (b) Calculated probability distributions of angle φ between the O–H bond of water and the surface normal of the interfacial water. Both angles are shown in the insets, and the interfacial water is defined as being within 4 Å of the metal surface (IHP). (c) Calculated probability distributions of angle φ between the water bisector and the surface normal of the interfacial water. (d) Profiles of dipole orientation of H_2O along the surface normal direction z at different potentials, where the zero corresponds to the location of the metal surface. (e) Statistical distribution of the H-bond number along surface normal direction. (f) Three-dimensional plot showing the relationship between proton transfer frequency, H-bonds length and different potentials. (g) pH dependence of the HER activities of 15% Co/O-FeP/MWCNTs. (h) Current densities of 15% Co/O-FeP/MWCNTs at −0.15 V versus RHE as a function of the pH value. (i) The free energy profile of PT-2 along the CV. Inset is the close-up of atomic structures evolution of the PT-1 to PT-2.

normal of the interfacial water, and angle φ between the O–H bond of water and the surface normal. At 1.12 V (PZC), φ is 67.8° and θ is 53°, indicating a predominant H-up configuration in the IHP. As the potential decreases to 0.76 and −0.16 V (RHE), φ (Fig. 6(b)) exhibits two peaks (88° and 160°), indicating a reorientation of water molecules within the electrical double layer (EDL), as shown in the inset. At 0.76 V (RHE), θ (Fig. 6(c)) also shows two peaks, suggesting the coexistence of both H-up and H-down configurations. The corresponding dipole orientations (cosθ, Fig. 6(b)) are 15° and 116°, further confirming the coexistence of both configurations. At −0.16 and −0.67 V, all interfacial water configurations reorient into a highly ordered, consistent with the O 1s XPS spectra (Fig. 4(d)). In this case, the dipole orientation in the IHP ranges from 128° to 132°, indicating the exclusive presence of the H-down configuration. The distribution of H-bond numbers along the surface normal direction (Fig. 6(e)) serves as an indicator of the connectivity within the interfacial HBN. At −0.67 V, a region approximately 9.5 Å from the 15% Co/O-FeP/MWCNTs (202) surface (red shaded area) exhibits a markedly lower number of hydrogen bonds than the neighboring regions.

Although water molecules in this region remain an H-down configuration, the HBN connectivity is disrupted, suggesting that proton transfer from the bulk to the catalytic interface critically depends on the continuity of the HBN. To elucidate the factors

influencing HBN connectivity, we analyzed H-bond lengths (Fig. S42 in the ESM) and PT frequencies (Fig. S43 in the ESM) at various potentials (Fig. 6(f)). From 0.76 to −0.16 V, the PT frequency increases with decreasing H-bond length. Notably, at −0.67 V, the PT frequency drops to 67, indicating that PT-1 becomes the RDS, in agreement with experimental KIE results. Research indicates that the HER likely constitutes a complex system. The catalyst performance is collectively governed by: (i) the ΔG_H at active sites, (ii) interfacial water configurations induced by interface charge distribution, and (iii) connectivity of the HBN. The PT-1 is governed by HBN connectivity, PT-2 is primarily influenced by the configuration of interfacial water molecules in the IHP. The above two steps determine the overall PT efficiency during HER. For 15% Co/O-FeP/MWCNTs demonstrates excellent HER performance, it must not only offer optimal ΔG_H, but also ensure efficient PT-1 and PT-2 through favorable interfacial electronic structure. This may also account for the observed differences in HER performance between acidic and alkaline media.

Based on the above conclusions, the specific roles that PT-1 and PT-2 play in HER have not yet been clarified. The metadynamics method was employed to simulate the free energy barriers of PT-1 and PT-2 to explore the kinetics of HER. In the PT-1 process, the collective variable (CV) is defined as the combination of several O–H distances connecting the H-bond networks from H_3O^+ to the closest water molecule (Fig. S44 in the ESM). To ensure the accuracy and reliability of the free energy barrier, the PT simulation of each water molecule was independently conducted three times for error analysis. In the acidic volmer step, the hydronium at OHP transfers H to the dissociated water molecules closest to the electrode surface through the H-bond networks in the EDL (Fig. S44 inset in the ESM). During the PT-1 process, protons jump back and forth between water molecules through the Grotthuss mechanism, with an average energy barrier of 0.004 eV and a time scale of fs. Although an obvious pH dependence was observed (Fig. 6(g)), this does not undermine the role of interfacial water configuration in governing the proton -transfer kinetics, according to the law of mass action. The H^+ concentration in solution mainly affects the amount of protons delivered to the catalyst interface, whereas the intrinsic rate of proton transfer is still dictated by the structure/configuration of water molecules at the interface. The relatively large ρ value (Fig. 6(h)) further supports this interpretation. In contrast, a small ρ would imply sluggish proton transfer, such that protons cannot be efficiently shuttled to (or across) the interface, leading to only a limited enhancement in the current density (J_{geo} (mA·cm^{-2})).

The proton desolvation shell of the volmer reaction (PT-2) at the acid interface was simulated by using the O–H bond length of the interfacial water molecule closest to the electrode surface as CV. In the PT-2 process (Fig. 6(i)), protons combine with interface water molecules to form H_3O^+, and the H2 alternately jumps between O2 and O3 (Fig. 6(i) inset). Simultaneously, the H3 desolvation and interface charge coupling form the CPET mechanism, and its activation energy (0.041 eV) is an order of magnitude larger than that of PT-1. The results show that when the connectivity of the HBN is not disrupted, the energy barrier of PT-1 is smaller than that of PT-2, meaning that PT-2 is an RDS. In this paper, PT-2 is RDS, so it is feasible to use ΔG_H to evaluate the quality of the catalyst. However, if PT1 is an RDS, ΔG_H as a descriptor to evaluate the quality of the catalyst is not applicable. HER is a PCET process, in which PT is influenced by multiple factors, including interfacial charge distribution, catalyst conductivity, and hydrogen-bond network connectivity. Previous studies using only a single evaluation criterion no longer accurately describe the properties of HER catalysts.

3 Conclusions

In summary, 15% Co/O-FeP/MWCNTs has been demonstrated as an efficient HER catalyst, achieving an ultralow overpotential of 58 mV at 10 mA·cm^{-2} and sustaining 500 mA·cm^{-2} for over 111 h in acidic media. Compared to CoP/MWCNTs and FeP/MWCNTs, the optimized d-band centre of 15% Co/O-FeP balances proton adsorption and desorption, enabling superior catalytic performance. It shows great promise for future industrial applications. Kinetic isotope effect measurements and *in-situ* EIS confirm that rapid PT within IHP is concertedly coupled with electron transfer, giving rise to a CPET pathway. Combining *in-situ* Raman spectroscopy with AIMD simulations, we further identify that H-down configurations of interfacial water molecules governs the frequency of PT evenets in the IHP. Mechanically, HER proceeds via two interconnected PT steps, namely HBN in the bulk electrolyte (PT-1) and interfacial water orientations within the IHP (PT-2), involving proton migration through the outer Helmholtz plane and the desovlation of H_3O^+. Under more negative potentials (e.g., −0.67 V), the bulk HBN becomes increasingly disrupted by field-induced H-bond shortening, which reduces its flexibility and suppresses efficient PT-1, even though the interfacial H-down configuration is retained. This work establishes a direct link between catalyst electronic structure, interfacial water orientation, and bulk HBN connectivity, showing how they collectively regulate proton transfer and the desolvation to trigger CPET. Theses insights advance the knowledge of PT dynamics, providing a comprehensive theoretical picture for HER. Beyond HER, the design principles highlighted here—engineering electronic structures while tailoring interfacial water and HBN offer the guidance for developing advanced catalysts for proton transfer involved reactions, such as selective semihydridation of alkynes to olefins.

Electronic Supplementary Material: Supplementary material (XPS full spectra, EPR spectra, SEM and TEM images of FeP/MWCNTs and CoP/MWCNTs; test device and reference electrode calibration for HER; HER performance of various Co/O-FeP/MWCNTs without *iR*-correction; catalyst synthesis method, HER test method, and theoretical calculation) is available in the online version of this article at https://doi.org/10.26599/NR.2026.94908648.

Data availability

All data needed to support the conclusions in the paper are presented in the manuscript and the Electronic Supplementary Material. Additional data related to this paper may be requested from the corresponding author upon request.

Acknowledgements

This work was supported by the National Natural Science Foundation of China (No. 52477219) and Science and technology Innovation Action Plan of Shanghai (No. 23DZ1200600). The authors also acknowledge the financial support from the 111 Project China (No. DT20015).

Declaration of competing interest

All the contributing authors report no conflict of interests in this work.

Author contribution statement

Y. F G.: Data curation, project administration, validation, writing manuscript, experimental design. J. Y. W., Y. S. Y., and L. W.: Data curation, project administration, validation, experimental design. A. M. Y., D.-s. L., and C. M. Z.: Project administration, writing manuscript. C. H. S.: Project administration, funding acquisition. H. L.: Project administration, funding acquisition, writing manuscript. All the authors have approved the final manuscript.

Use of AI statement

None.

References

[1] Roger, I.; Shipman, M. A.; Symes, M. D. Earth-abundant catalysts for electrochemical and photoelectrochemical water splitting. *Nat. Rev. Chem.* **2017**, *1*, 0003.

[2] Kibsgaard, J.; Chorkendorff, I. Considerations for the scaling-up of water splitting catalysts. *Nat. Energy* **2019**, *4*, 430–433.

[3] Yuan, S.; Peng, J. Y.; Cai, B.; Huang, Z. H.; Garcia-Esparza, A. T.; Sokaras, D.; Zhang, Y. R.; Giordano, L.; Akkiraju, K.; Zhu, Y. G. et al. Tunable metal hydroxide-organic frameworks for catalysing oxygen evolution. *Nat. Mater.* **2022**, *21*, 673–680.

[4] Tymoczko, J.; Calle-Vallejo, F.; Schuhmann, W.; Bandarenka, A. S. Making the hydrogen evolution reaction in polymer electrolyte membrane electrolysers even faster. *Nat. Commun.* **2016**, *7*, 10990.

[5] Liu, D.; Xu, G. Y.; Yang, H.; Wang, H. T.; Xia, B. Y. Rational design of transition metal phosphide-based electrocatalysts for hydrogen evolution. *Adv. Funct. Mater.* **2023**, *33*, 2208358.

[6] Liu, B. Y.; Lan, X. C.; Zhong, Q.; Wang, T. F. Metal phosphide: An atypical catalytic site. *ACS Catal.* **2024**, *14*, 757–775.

[7] Wang, K.; Huang, B. L.; Lin, F.; Lv, F.; Luo, M. C.; Zhou, P.; Liu, Q.; Zhang, W. Y.; Yang, C.; Tang, Y. H. et al. Wrinkled Rh_2P Nanosheets as superior pH-universal electrocatalysts for hydrogen evolution catalysis. *Adv. Energy Mater.* **2018**, *8*, 1801891.

[8] Mushtaq, N.; Ma, X. L.; Aslam, K.; Younas, W.; Zhu, Y. Q.; Cao, C. B. Synthesis of ultrathin porous bimetallic nickel–cobalt phosphide nanosheets as an excellent bifunctional electrocatalyst for overall water splitting. *Energy Technol.* **2022**, *10*, 2200537.

[9] Jiang, M.; Zhai, H. H.; Chen, L. B.; Mei, L.; Tan, P. F.; Yang, K.; Pan, J. Unraveling the synergistic mechanism of bi-functional nickel–iron phosphides catalysts for overall water splitting. *Adv. Funct. Mater.* **2023**, *33*, 2302621.

[10] Zhang, K.; Jia, J.; Yang, E. D.; Qi, S. P.; Tian, H. Z.; Chen, J. X.; Li, J.; Lou, Y. B.; Guo, Y. Z. Work-function-induced electron rearrangement of in-plane FeP@CoP heterojunction enhances all pH range and alkaline seawater hydrogen evolution reaction. *Nano Energy* **2023**, *114*, 108601.

[11] Jiang, H. L.; Zhao, Z.; Li, G.; Wang, M. X.; Chen, P. H.; Liu, X. T.; Tu, X. M.; Hu, Y. T.; Shen, Z.; Wu, Y. R. Hollow spherical heterostructured FeCo–P catalysts derived from MOF-74 for efficient overall water splitting. *Adv. Sci.* **2024**, *11*, 2306919.

[12] Hammes-Schiffer, S. Introduction: Proton-coupled electron transfer. *Chem. Rev.* **2010**, *110*, 6937–6938.

[13] Bonin, J.; Costentin, C.; Robert, M.; Routier, M.; Savéant, J. M. Proton-coupled electron transfers: pH-dependent driving forces? Fundamentals and artifacts. *J. Am. Chem. Soc.* **2013**, *135*, 14359–14366.

[14] Weinberg, D. R.; Gagliardi, C. J.; Hull, J. F.; Murphy, C. F.; Kent, C. A.; Westlake, B. C.; Paul, A.; Ess, D. H.; McCafferty, D. G.; Meyer, T. J. Proton-coupled electron transfer. *Chem. Rev.* **2012**, *112*, 4016–4093.

[15] Jackson, M. N.; Jung, O.; Lamotte, H. C.; Surendranath, Y. Donor-dependent promotion of interfacial proton-coupled electron transfer in aqueous electrocatalysis. *ACS Catal.* **2019**, *9*, 3737–3743.

[16] Liu, T. F.; Tyburski, R.; Wang, S. H.; Fernández-Terán, R.; Ott, S.; Hammarström, L. Elucidating proton-coupled electron transfer mechanisms of metal hydrides with free energy- and pressure-dependent kinetics. *J. Am. Chem. Soc.* **2019**, *141*, 17245–17259.

[17] Qiao, C.; Usman, Z.; Wei, J.; Gan, L.; Hou, J. H.; Hao, Y. Y.; Zhu, Y. Q.; Zhang, J. T.; Cao, C. B. Efficient O–O coupling at catalytic interface to assist kinetics optimization on concerted and sequential proton-electron transfer for water oxidation. *ACS Nano* **2023**, *17*, 12278–12289.

[18] Jackson, M. N.; Surendranath, Y. Donor-dependent kinetics of interfacial proton-coupled electron transfer. *J. Am. Chem. Soc.* **2016**, *138*, 3228–3234.

[19] Dey, S.; Masero, F.; Brack, E.; Fontecave, M.; Mougel, V. Electrocatalytic metal hydride generation using CPET mediators. *Nature* **2022**, *607*, 499–506.

[20] Kaminsky, C. J.; Weng, S.; Wright, J.; Surendranath, Y. Adsorbed cobalt porphyrins act like metal surfaces in electrocatalysis. *Nat. Catal.* **2022**, *5*, 430–442.

[21] Elgrishi, N.; McCarthy, B. D.; Rountree, E. S.; Dempsey, J. L. Reaction pathways of hydrogen-evolving electrocatalysts: Electrochemical and spectroscopic studies of proton-coupled electron transfer processes. *ACS Catal.* **2016**, *6*, 3644–3659.

[22] Darcy, J. W.; Koronkiewicz, B.; Parada, G. A.; Mayer, J. M. A Continuum of proton-coupled electron transfer reactivity. *Acc. Chem. Res.* **2018**, *51*, 2391–2399.

[23] Li, P.; Jiang, Y. L.; Hu, Y. C.; Men, Y.; Liu, Y. W.; Cai, W. B.; Chen, S. L. Hydrogen bond network connectivity in the electric double layer dominates the kinetic pH effect in hydrogen electrocatalysis on Pt. *Nat. Catal.* **2022**, *5*, 900–911.

[24] Shen, L. F.; Lu, B. A.; Li, Y. Y.; Liu, J.; Huang-fu, Z. C.; Peng, H.; Ye, J. Y.; Qu, X. M.; Zhang, J. M.; Li, G. et al. Interfacial structure of water as a new descriptor of the hydrogen evolution reaction. *Angew. Chem., Int. Ed.* **2020**, *59*, 22397–22402.

[25] Dereka, B.; Yu, Q.; Lewis, N. H. C.; Carpenter, W. B.; Bowman, J. M.; Tokmakoff, A. Crossover from hydrogen to chemical bonding. *Science* **2021**, *371*, 160–164.

[26] Guo, R. X.; Zhou, Y. C.; Wang, W.; Zhai, Y. M.; Liu, X. F.; He, W. J.; Ou, W.; Ding, R.; Zhang, H. L.; Wu, M. L. et al. Interlayer confinement toward short hydrogen bond network construction for fast hydroxide transport. *Sci. Adv.* **2025**, *11*, eadr5374.

[27] Zhou, S. Q.; Cao, W.; Shang, L.; Zhao, Y. X.; Xiong, X. Y.; Sun, J. K.; Zhang, T. R.; Yuan, J. Y. Facilitating alkaline hydrogen evolution kinetics via interfacial modulation of hydrogen-bond networks by porous amine cages. *Nat. Commun.* **2025**, *16*, 1849.

[28] Wang, P. Y.; Zhou, J. F.; Chen, H.; Peng, B.; Zhang, K. Activation of H_2O tailored by interfacial electronic states at a nanoscale interface for enhanced electrocatalytic hydrogen evolution. *JACS Au* **2022**, *2*, 1457–1471.

[29] Zhai, Y. Y.; Ren, X. R.; Sun, Y.; Li, D.; Wang, B. L.; Liu, S. Z. Synergistic effect of multiple vacancies to induce lattice oxygen redox in NiFe-layered double hydroxide OER catalysts. *Appl. Catal. B: Environ.* **2023**, *323*, 122091.

[30] Huang, G. Q.; Zhao, L.; Yuan, S. S.; Li, N.; Jing, S. B. Iron doped mesoporous cobalt phosphide with optimized electronic structure for enhanced hydrogen evolution. *Int. J. Hydrogen Energy* **2022**, *47*, 14767–14776.

[31] Xiao, Z. H.; Huang, Y. C.; Dong, C. L.; Xie, C.; Liu, Z. J.; Du, S. Q.; Chen, W.; Yan, D. F.; Tao, L.; Shu, Z. W. et al. *Operando* identification of the dynamic behavior of oxygen vacancy-rich Co_3O_4

for oxygen evolution reaction. *J. Am. Chem. Soc.* **2020**, *142*, 12087–12095.

[32] Shi, Z. P.; Wang, Y.; Li, J.; Wang, X.; Wang, Y. B.; Li, Y.; Xu, W. L.; Jiang, Z.; Liu, C. P.; Xing, W. et al. Confined Ir single sites with triggered lattice oxygen redox: Toward boosted and sustained water oxidation catalysis. *Joule* **2021**, *5*, 2164–2176.

[33] Chen, B. Y.; Dobele, G.; Plavniece, A.; Volperts, A.; Tamasauskaite-Tamasiunaite, L.; Norkus, E.; Chen, C. L.; Lin, Y. C. Catalytic hydrogenation of CO_2 to light olefins by using K-doped FeC_x catalysts derived from the Fe-chitosan complex. *Int. J. Hydrogen Energy* **2023**, *48*, 4276–4286.

[34] Qu, Q. Y.; Ji, S. F.; Chen, Y. J.; Wang, D. S.; Li, Y. D. The atomic-level regulation of single-atom site catalysts for the electrochemical CO_2 reduction reaction. *Chem. Sci.* **2021**, *12*, 4201–4215.

[35] Gao, R. J.; Pan, L.; Wang, H. W.; Zhang, X. W.; Wang, L.; Zou, J. J. Ultradispersed nickel phosphide on phosphorus-doped carbon with tailored d-band center for efficient and chemoselective hydrogenation of nitroarenes. *ACS Catal.* **2018**, *8*, 8420–8429.

[36] Sun, S. F.; Zhou, X.; Cong, B. W.; Hong, W. Z.; Chen, G. Tailoring the d-band centers endows $(Ni_xFe_{1-x})_2P$ nanosheets with efficient oxygen evolution catalysis. *ACS Catal.* **2020**, *10*, 9086–9097.

[37] Nørskov, J. K.; Abild-Pedersen, F.; Studt, F.; Bligaard, T. Density functional theory in surface chemistry and catalysis. *Proc. Natl. Acad. Sci. USA* **2011**, *108*, 937–943.

[38] Hammer, B.; Nørskov, J. K. Theoretical surface science and catalysis-calculations and concepts. *Adv. Catal.* **2000**, *45*, 71–129.

[39] Feng, Y. Q.; Wei, Y.; Wu, B.; Li, J. N.; Dong, Q.; Li, X.; Wang, Y.; Liu, Q. Q.; Ma, Q. Z.; Zhang, J. et al. Tuning *D*-band electronic interaction between Pt and Ru confined in fullerene network accelerate hydrogen spillover for efficient and pH-universal hydrogen evolution. *Adv. Energy Mater.* **2025**, *15*, e03878.

[40] Knyazev, Y. V.; Kazak, N. V.; Zhandun, V. S.; Bartolomé, J.; Arauzo, A.; Belskaya, N. A.; Bayukov, O. A.; Bezmaternykh, L. N.; Ovchinnikov, S. G. Electronic and magnetic states of Fe ions in Co_2FeBO_5. *Dalton Trans.* **2021**, *50*, 9735–9745.

[41] Oku, M.; Hirokawa, K. X-ray photoelectron spectroscopy of Co_3O_4, Fe_3O_4, Mn_3O_4, and related compounds. *J. Electron. Spectrosc. Relat. Phenom.* **1976**, *8*, 475–481.

[42] Huang, J. Z.; Wang, R.; Sheng, H. Y.; Zhu, X. R.; Dominic Ross, R.; Hua, D. X.; Lin, L.; Li, Y. F.; Zhang, Q. H.; Gu, L. et al. Isotope-dependent Tafel analysis probes proton transfer kinetics during electrocatalytic water splitting. *Nat. Chem.*, in press, DOI: 10.1038/s41557-025-01934-5.

[43] Zhou, H. Y.; Duan, X. G.; Huang, B. K.; Zhong, S.; Cheng, C.; Sharma, V. K.; Wang, S. B.; Lai, B. Isotope techniques in chemical wastewater treatment: Opportunities and uncertainties. *Angew. Chem., Int. Ed.* **2025**, *64*, e202422892.

[44] Wang, T.; Zhang, Y. R.; Huang, B. T.; Cai, B.; Rao, R. R.; Giordano, L.; Sun, S. G.; Shao-Horn, Y. Enhancing oxygen reduction electrocatalysis by tuning interfacial hydrogen bonds. *Nat. Catal.* **2021**, *4*, 753–762.

[45] Berg, N.; Bergwinkl, S.; Nuernberger, P.; Horinek, D.; Gschwind, R. M. Extended hydrogen bond networks for effective proton-coupled electron transfer (PCET) reactions: The unexpected role of thiophenol and its acidic channel in photocatalytic hydroamidations. *J. Am. Chem. Soc.* **2021**, *143*, 724–735.

[46] Wang, Y. R.; Liu, M.; Gao, G. K.; Yang, Y. L.; Yang, R. X.; Ding, H. M.; Chen, Y.; Li, S. L.; Lan, Y. Q. Implanting numerous hydrogen-bonding networks in a Cu-porphyrin-based nanosheet to boost CH_4 selectivity in neutral-media CO_2 electroreduction. *Angew. Chem., Int. Ed.* **2021**, *60*, 21952–21958.

[47] Chen, X.; Wang, X. T.; Le, J. B.; Li, S. M.; Wang, X.; Zhang, Y. J.; Radjenovic, P.; Zhao, Y.; Wang, Y. H.; Lin, X. M. et al. Revealing the role of interfacial water and key intermediates at ruthenium surfaces in the alkaline hydrogen evolution reaction. *Nat. Commun.* **2023**, *14*, 5289.

[48] Cheng, T.; Shen, D. X.; Meng, M.; Mallick, S.; Cao, L. J.; Patmore, N. J.; Zhang, H. L.; Zou, S. F.; Chen, H. W.; Qin, Y. et al. Efficient electron transfer across hydrogen bond interfaces by proton-coupled and -uncoupled pathways. *Nat. Commun.* **2019**, *10*, 1531.

[49] Li, J. Y.; Hu, J.; Zhang, M. K.; Gou, W. Y.; Zhang, S.; Chen, Z.; Qu, Y. Q.; Ma, Y. Y. A fundamental viewpoint on the hydrogen spillover phenomenon of electrocatalytic hydrogen evolution. *Nat. Commun.* **2021**, *12*, 3502.

[50] Chen, W.; Wu, B. B.; Wang, Y. Y.; Zhou, W.; Li, Y. Y.; Liu, T. Y.; Xie, C.; Xu, L. T.; Du, S. Q.; Song, M. L. et al. Deciphering the alternating synergy between interlayer Pt single-atom and NiFe layered double hydroxide for overall water splitting. *Energy Environ. Sci.* **2021**, *14*, 6428–6440.

[51] Li, C. Y.; Le, J. B.; Wang, Y. H.; Chen, S.; Yang, Z. L.; Li, J. F.; Cheng, J.; Tian, Z. Q. *In situ* probing electrified interfacial water structures at atomically flat surfaces. *Nat. Mater.* **2019**, *18*, 697–701.